Measurement Science
and Technology

PURPOSE-LED
PUBLISHING™

ACCEPTED MANUSCRIPT • OPEN ACCESS

Revisiting rotating bending fatigue in FFF polymer specimens using geometry-based cross-section properties for stress estimation

To cite this article before publication: Carolina Bermudo Gamboa *et al* 2026 *Meas. Sci. Technol.* in press https://doi.org/10.1088/1361-6501/ae5997

Manuscript version: Accepted Manuscript

Accepted Manuscript is "the version of the article accepted for publication including all changes made as a result of the peer review process, and which may also include the addition to the article by IOP Publishing of a header, an article ID, a cover sheet and/or an 'Accepted Manuscript' watermark, but excluding any other editing, typesetting or other changes made by IOP Publishing and/or its licensors"

This Accepted Manuscript is **© 2026 The Author(s). Published by IOP Publishing Ltd**.

As the Version of Record of this article is going to be / has been published on a gold open access basis under a CC BY 4.0 licence, this Accepted Manuscript is available for reuse under a CC BY 4.0 licence immediately.

Everyone is permitted to use all or part of the original content in this article, provided that they adhere to all the terms of the licence https://creativecommons.org/licences/by/4.0

Although reasonable endeavours have been taken to obtain all necessary permissions from third parties to include their copyrighted content within this article, their full citation and copyright line may not be present in this Accepted Manuscript version. Before using any content from this article, please refer to the Version of Record on IOPscience once published for full citation and copyright details, as permissions may be required. All third party content is fully copyright protected and is not published on a gold open access basis under a CC BY licence, unless that is specifically stated in the figure caption in the Version of Record.

View the article online for updates and enhancements.

This content was downloaded from IP address 46.25.249.8 on 13/04/2026 at 16:52

Revisiting Rotating Bending Fatigue in FFF Polymer Specimens Using Geometry-Based Cross-Section Properties for Stress Estimation

Carolina Bermudo Gamboa*, Fermín Bañón García, Sergio Martín-Béjar, José Andrés López-Fernández*
Department of Civil, Materials, and Manufacturing Engineering, University of Málaga, 29071 Málaga, Spain
bgamboa@uma.es*, fbanon@uma.es, smartinb@uma.es, alopezf@uma.es*

*Corresponding authors

Abstract

The fatigue performance of polymer components fabricated by Fused Filament Fabrication (FFF) under cyclic loading is strongly influenced by their shell-infill configuration. Standard rotating bending fatigue procedures, such as ISO 1143:2010, assume solid and homogeneous circular sections, which can bias stress estimations when applied to FFF specimens. In the absence of a specific fatigue standard for additively manufactured polymers, this work compares four analytical approaches to calculate the section modulus and associated moment of inertia of FFF-printed specimens subjected to rotating bending fatigue tests, enabling accurate estimation of the maximum surface stress through the classical flexural relation. The approaches range from the solid-section assumption to an Analytical Geometry-Based (AGB) formulation that represents horizontally printed morphologies with ovalized shell-infill interfaces and non-uniform shell thickness. The impact of each approach is assessed by reconstructing S–N curves using (i) new rotating bending tests on PLA specimens manufactured with grid and honeycomb infill patterns and varying infill density under constant bending moment, and (ii) literature data recalculated using geometry-aware section properties. Reprocessing published PLA datasets shows that geometry-aware stress estimation in some cases can approximately double the inferred fatigue life relative to ISO-based calculations. Experimentally, grid infill provides longer fatigue lives than honeycomb under otherwise identical conditions. Overall, the AGB approach provides the most consistent stress estimation for horizontally printed cylinders and improves the comparability of rotating bending fatigue results across different FFF configurations.

Keywords: Fused filament fabrication (FFF); Rotating bending fatigue; Stress estimation; Geometry-based approach; Anisotropy; S–N curves

1. Introduction

Additive manufacturing (AM) techniques, particularly Fused Filament Fabrication (FFF), have become widespread in the fabrication of polymer components due to their low cost, material efficiency, and geometric versatility [1,2]. Their ability to produce complex geometries without tooling has enabled successful implementation in diverse fields such as medicine, where patient-specific prosthetics and anatomical models are routinely fabricated; aerospace, where lightweight polymeric supports and housings reduce part count and cost; and automotive, among others, where functional prototypes and custom fixtures benefit from reduced lead times and design flexibility [3–6]. In many of these cases, FFF offers clear advantages over subtractive and injection molding processes, particularly in terms of design freedom, material efficiency, and turnaround time. Its layer-by-layer deposition approach allows for greater flexibility in shape customization and faster iteration cycles, which is especially beneficial during the development of physical prototypes [7]. Furthermore, it enables the fabrication of complex geometries—such as molds with integrated internal channels—that would be costly or unfeasible using traditional machining or molding techniques [8]. These characteristics make FFF highly

Accepted Manuscript

suitable for customized or small-batch production scenarios, where conventional injection molding becomes economically inefficient due to tooling costs and setup times [9].

Despite these benefits, the mechanical performance of FFF parts remains a major limitation for their structural application. Unlike conventionally manufactured components, FFF parts are composed, in general, of a continuous outer shell and an internal region formed by a periodic infill pattern with controlled porosity. This architecture results in cross-sections that are both non-homogeneous and anisotropic, with mechanical properties highly dependent on printing parameters such as infill density, shell thickness, raster orientation, and layer height. The influence of these parameters has been widely documented: raster angle configurations can significantly impact tensile and bending strength, with common orientations such as 0°/90° or ±30° directly affecting mechanical behavior [10]. The extrusion flow rate also plays a critical role, where proper calibration can eliminate internal voids and increase Z-direction tensile strength by up to 50%, reducing anisotropy [11]. Similarly, layer orientation affects porosity and strength, with certain configurations—such as XY printing combined with thermal treatment—achieving a 14% improvement in mechanical resistance [12].

Infill density and shell configuration have also been shown to govern mechanical anisotropy [13], and even quasi-isotropic deposition patterns in short-fiber reinforced materials do not eliminate anisotropic behavior, due to filament microstructure and porosity [14]. Fatigue life is particularly sensitive to layer and raster orientation: some raster configurations can suppress the transition phase in fatigue failure [15], while perpendicular rasters have been reported to reduce tensile and fatigue strength by up to 18% [16]. Overall, these findings confirm that the mechanical response of FFF parts—tensile strength, stiffness, fracture toughness, impact resistance, and fatigue behavior—differs markedly from that of bulk materials with the same nominal composition, due to the microstructural and geometric complexity introduced by the printing process.

In conventionally manufactured metallic materials, fatigue life is generally treated as an intrinsic property of the material. Under standardized test conditions, such as those defined in ISO 1143, the number of cycles to failure can be reliably predicted for a given stress level, independent of the specific geometry of the specimen. This is possible because metallic components typically exhibit homogeneous and isotropic microstructures, and the influence of factors such as surface finish or size is either minimal or can be accounted for through well-established correction factors. In contrast, FFF components exhibit complex, anisotropic internal architectures and layer-dependent properties that strongly couple fatigue life with geometry and process parameters. This makes the fatigue behavior of FFF polymers inherently more variable and difficult to generalize.

Among the various mechanical properties relevant to FFF components, rotating bending fatigue behavior has received comparatively less attention in scientific literature, despite its significance for components subjected to cyclic loading. In the limited studies that do examine this type of loading, rotating bending tests are commonly employed due to their simplicity and standardization. However, these tests are often conducted in accordance with ISO 1143:2010, a standard originally developed for metallic materials with fully solid, isotropic, and circular cross-sections. The direct application of this standard to FFF-printed polymers is problematic, as it assumes homogeneous material behavior and neglects the internal structural complexity introduced by additive manufacturing processes.

Several authors have highlighted these limitations. Travieso-Rodriguez et al. [17] showed that infill density and layer height have a strong influence on fatigue life in PLA-wood composites, illustrating the inadequacy of directly applying ISO 1143 to such materials. Brčić et al. [18] similarly noted the absence of standardized

Accepted Manuscript

models suitable for 3D-printed anisotropic polymers like PLA, ABS, and ASA in rotating bending conditions. Hassanifard and Hashemi [15] demonstrated that the transition from tensile to rotating bending loading significantly alters fatigue coefficients in PLA, underlining the insufficiency of isotropic-based standards for FFF. Nagengast et al. [19] further supported this by validating anisotropic behavior models using ISO 178, emphasizing the limitations of standards developed for homogeneous materials.

Additional modeling efforts reinforce these concerns. Dialami et al. [13] used a hybrid numerical-experimental strategy to differentiate the mechanical contributions of the isotropic shell and anisotropic infill, showing that assuming cross-sectional homogeneity introduces errors in fatigue prediction. Adibeig et al. [16], through FEM simulation, demonstrated that raster orientation and notch presence critically affect fatigue life, again exposing the mismatch with ISO 1143 assumptions. Finally, Cerda-Avila et al. [20] emphasized that conventional fatigue models fail to capture the real behavior of FFF parts if internal structure and process parameters are not accounted for. However, these approaches do not explicitly provide a closed-form section-property formulation that captures the characteristic morphology of horizontally printed cylindrical specimens, where the shell-infill interface becomes ovalized and the effective shell thickness varies around the perimeter. In such specimens, these two geometric features directly alter the local load-bearing area and the moment of inertia governing the maximum outer-fiber stress. The proposed AGB formulation addresses this specific gap by analytically representing the ovalized interface and the resulting non-uniform shell thickness, enabling stress estimation tied to the measured cross-sectional morphology without requiring case-specific finite element modeling.

As a consequence, directly applying ISO 1143 for stress estimation in FFF specimens introduces significant inaccuracies—particularly in parts with low infill percentages or irregular shell geometries—and fails to represent the anisotropic, non-homogeneous nature of printed cross-sections. This highlights the need for alternative analytical approaches that reflect the actual geometry and material distribution of FFF components in fatigue applications.

To address this limitation, the present work proposes the development and comparative analysis of four analytical approaches to estimate the moment of inertia I and resulting stress of FFF-printed cylindrical specimens subjected to rotating bending fatigue. Each estimation method introduces a different level of geometric fidelity: from the conventional solid-section approximation defined in ISO 1143 (Method 1), to progressively refined approaches that incorporate the role of the infill (Method 2), the combined contribution of shell and core (Method 3), and finally a method based on the real printed morphology of the section, including ovalized shell–infill interfaces and non-uniform shell thickness (Method 4, AGB). These methods are used to predict S–N curves and are compared against both experimental results obtained in this study and fatigue data from literature. The aim is to assess the ability of each method to capture the influence of internal geometry on fatigue performance, and to establish a robust framework for stress estimation in FFF components beyond the limitations of current standards. The AGB method is shown to provide improved agreement with experimental observations, offering a practical framework for fatigue life prediction in FFF-printed components based on their actual geometry.

The novelty of this work lies in providing a geometry-aware, fully analytical framework to estimate cross-section properties for rotating bending stress calculation in FFF specimens, explicitly accounting for the shell–infill geometry. While the bending stress relation is classical, the proposed contribution is the progressive modeling of the effective load-bearing section with increasing geometric fidelity. In addition, the study quantifies the practical impact of these geometric assumptions by showing that conventional solid-section

Accepted Manuscript

assumptions can introduce non-negligible bias in stress levels and the resulting fatigue-life interpretation. In particular, the AGB approach provides an analytical representation of the non-ideal printed section in horizontally printed cylinders, enabling stress estimation without relying on finite element modeling and improving comparability of S–N data across printing configurations.

2. Theoretical framework

2.1. Determination of rotating bending fatigue life in metals

Rotating bending fatigue testing is a standardized method used to evaluate the fatigue life of metallic materials under cyclic loading. The procedure is defined in standard ISO 1143:2010 [21], which specifies that specimens with a solid cylindrical geometry are subjected to a fully reversed cyclic bending moment while rotating around their longitudinal axis (Figure 1). This results in alternating tensile and compressive stresses on the specimen surface, with a stress ratio R = -1.

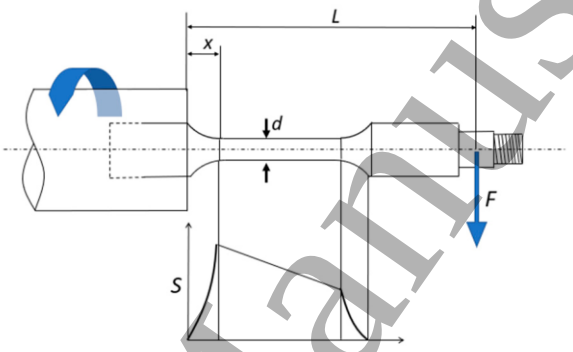

Figure 1. Fatigue test and stress distribution [22]

The test is performed using hourglass-shaped specimens designed to localize failure within a well-defined gauge section. The maximum stress (S_{max}), which is located at the surface, is determined by the bending moment M and the geometry of the cross-section, typically using the flexural equation:

$$S_{max} = \frac{M}{W} \quad \text{Eq. 1}$$

where W is the section modulus at the failure cross-section. For a solid circular section, this modulus is given by:

$$W = \frac{I}{r} = \frac{\pi d^4}{64} \cdot \frac{2}{d} = \frac{\pi d^3}{32} \quad \text{Eq. 2}$$

Alternatively, S_{max} can be calculated based on the applied force F, the lever arm length x, and the section modulus W, according to:

$$S_{max} = \frac{F \cdot x}{W} \quad \text{Eq. 3}$$

Here, I is the second moment of area (moment of inertia) of the section, and r is the outer radius at the gauge section. Once the maximum stress is determined, it is paired with the number of cycles to failure N to generate the S–N curve, which characterizes the material's fatigue response.

This method relies on several key assumptions: the specimen has a solid and homogeneous structure, the cross-section is circular and constant along the gauge zone, and the material is isotropic and has uniform distribution.

Accepted Manuscript

These assumptions are valid for conventional metallic specimens, but they do not hold for components manufactured via fused filament fabrication (FFF) or other additive manufacturing (AM) technologies.

In FFF printed specimens, the cross-sectional geometry is often non-solid and anisotropic, depending on the build orientation, infill density, and number of outer shells. The presence of an internal matrix or partially filled core significantly alters the moment of inertia I and the section modulus W. Therefore, directly applying ISO 1143 to such components, without accounting for these features, leads to a miscalculation of the actual maximum stress and a distortion of the resulting S–N curve. While ISO 1143 provides a robust framework for metals, its application to AM parts—particularly those produced by FFF—requires careful reinterpretation of the cross-sectional geometry and material distribution, as explored in subsequent sections of this work.

2.2. Morphology of cylindrical parts in additive manufacturing

The AM processes, specifically FFF for this case study, introduce unique geometric characteristics to printed components that significantly differentiate them from conventionally machined or molded parts. One of the most relevant structural distinctions in FFF specimens is the inherent dual composition of their cross-sections: the outer shell (or contour) and the infill.

The shell can be simplified to a set composed of solid, continuous extruded lines that define the external surface of the part. It also depends on several variables such as the number of shells, or the superposition percentage of the lines extruded, among others. In contrast, the infill is generated as a patterned, often non-continuous lattice structure whose material density is governed by a user-defined parameter known as the infill density factor (*fi*). When $f_i = 100\%$, the infill region can be considered as completely solid. In a cylindrical part, it results in a monolithic cross-section similar to a traditionally machined part. However, if $f_i < 100\%$, internal voids are intentionally introduced and the structure becomes heterogeneous, alternating zones of solid material and air gaps.

Furthermore, the deposition of material in FFF is inherently discrete and anisotropic. Filament is laid down layer by layer in the XY-plane, with subsequent layers stacked along the Z-axis. This discrete layering causes the material to behave differently in directions parallel and perpendicular to the printing layers, introducing anisotropy into both mechanical performance and geometric definition.

Among the most critical parameters in the printing process of a cylindrical part is its orientation on the build platform. In particular, how the cylindrical axis of the specimen aligns with the printer's coordinate system. This orientation dictates the direction of the extruded layers and, consequently, the internal structure and effective geometry of the cross-section. In this regard, there are two particularly common configurations employed in additive manufacturing: vertical printing, and horizontal printing. Each of these orientations results in different structural and geometric characteristics that significantly influence the final mechanical performance of the printed specimen.

In the case of vertically printed cylinders, where the longitudinal axis of the specimen is aligned with the printer's Z-axis, the cross-sectional plane perpendicular to the loading axis retains a circular shape. The external contour (shell) and the transition between shell and infill follow circular profiles, and the shell thickness remains constant along the perimeter (Figure 2a). Although this configuration yields more geometrically homogeneous sections, it tends to perform poorly under tensile or bending loads. Failure in vertically printed specimens commonly occurs by delamination, i.e., the separation between layers, due to the weak inter-layer adhesion

Accepted Manuscript

along the build direction. Figure 3a and 3b show two vertically printed specimens, without a shell and with a 3-layer shell respectively.

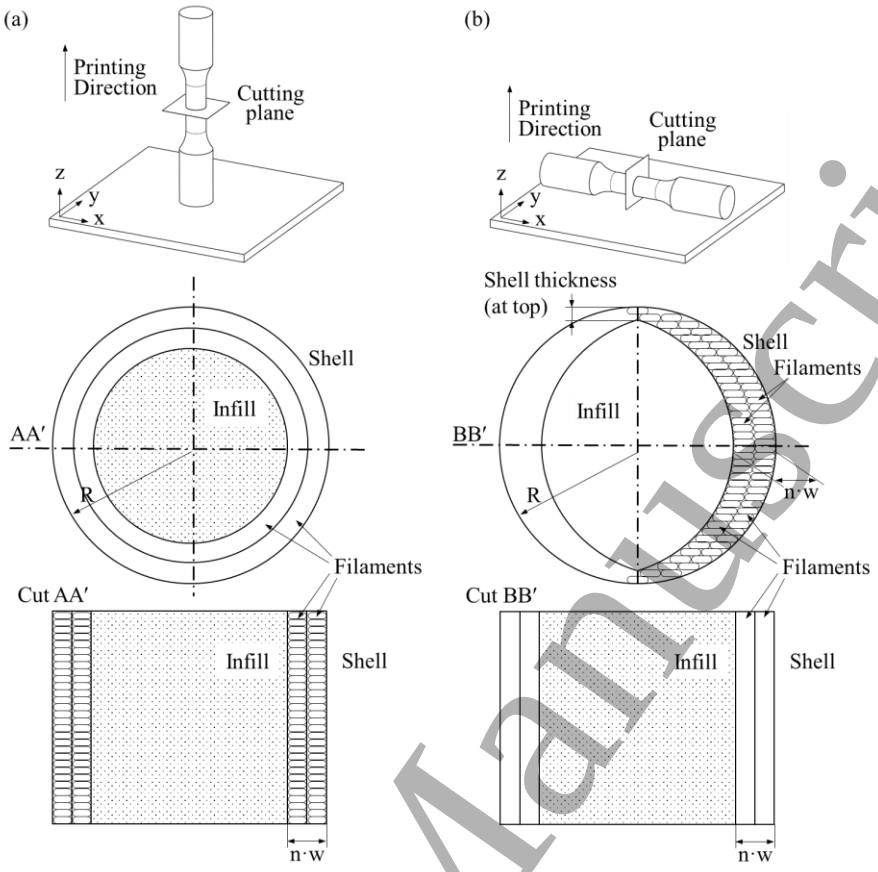

Figure 2. Cylindrical FFF specimen representation printed along different orientations: (a) vertical and (b) horizontal.

In contrast, when the cylinder is printed horizontally, as schematically represented in Figure 2b, i.e. with its longitudinal axis lying on the XY-plane, the cross-sectional profile is no longer strictly circular. Due to the layered construction and slicing resolution, the interface between the shell and the infill becomes oval, and the effective shell thickness is no longer uniform around the perimeter, as observed in the printed samples with different infill factor shown in Figure 4. The result is a non-homogeneous section where the load-carrying capacity varies depending on angular position. Under tensile or bending loading, the failure mode in horizontally printed parts is governed by material fracture rather than delamination, which generally allows them to withstand higher stress levels. As a result, this orientation is commonly preferred for cylindrical parts when mechanical performance under loading is a critical factor.

Accepted Manuscript

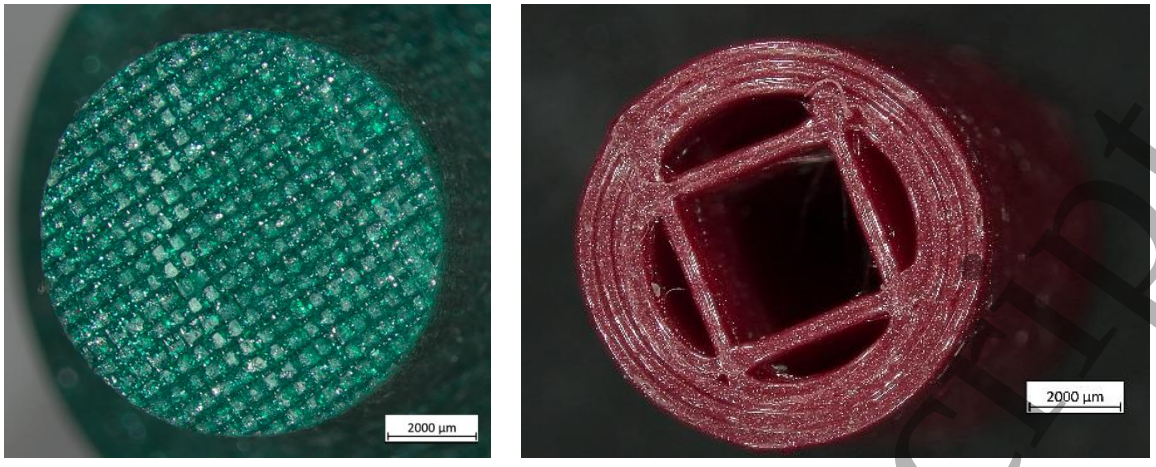

(a) (b)

Figure 3. Vertically printed PLA specimens: (a) 100% infill after rotating-bending fatigue testing; (b) 25% infill with a rectangular pattern and three layers, obtained by interrupting the manufacturing process to expose the gauge section, shown in the as-printed condition.

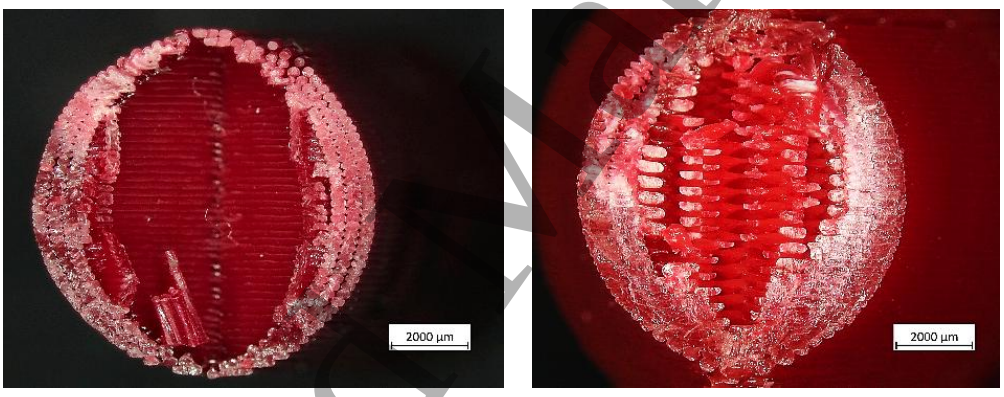

(a) (b)

Figure 4. Horizontally printed PLA specimens after rotating-bending fatigue testing: (a) 3 shells, 0.2 mm layer height, 25% infill; (b) 2 shells, 0.3 mm layer height, 50% infill [23].

This variability becomes particularly relevant in rotating bending fatigue tests. In such tests, the cyclic stress distribution is highly sensitive to cross-sectional geometry. Assuming a homogeneous solid circular section, as prescribed by the ISO 1143:2010 [21] standard, can lead to substantial inaccuracies in calculating the maximum bending stress (S_{max}), especially when the actual section includes internal voids and non-uniform shell thicknesses.

In horizontally printed FFF specimens, the actual geometry of the cross-section depends not only on the number of outer shells (n) but also on the extrusion width (ω) and the fi. A simplified model of the cross-section can be considered as a solid external ring of thickness $n\omega$, representing the shell, and a core region with reduced effective stiffness, influenced by the chosen infill pattern and density (Figure 4).

Accepted Manuscript

Therefore, accurate interpretation of rotating bending fatigue in FFF parts requires the characterization of the cross-section. Accordingly, applying ISO 1143 [21] without correcting for the actual printed morphology may bias stress estimation and the resulting fatigue-life assessment.

2.3. Problem statement: Determination of rotating bending fatigue life in additive manufacturing

In the context of FFF and considering the material distribution within the specimen, two sources of error have been identified:

On the one hand, the shell and the infill geometry and material distribution depend on user-defined parameters such as n, ω or fi. Although for a value of $f_i = 100\%$ the specimen can be considered fully solid, and the assumptions of the ISO standard are reasonably satisfied, values of $f_i < 100\%$ cause the presence of internal voids which significantly reduces the density, effective stiffness and, consequently, the load-bearing capacity of the cross-section. In such cases, using the inertia of a full solid section overestimates the section's moment resistance, resulting in an underestimation of S and a distortion in the derived fatigue life. To address this limitation, the current study introduces a methodology that accounts for the actual geometry and material distribution within the cross-section. Specifically, the total moment of inertia of the section I_{total} is modeled as the sum of two components:

$$I_{total} = I_{shell} + I_{infill} \quad \text{Eq. 4}$$

where I_{shell} corresponds to the moment of inertia of the external ring which depends on $n\omega$, *and* I_{infill} represents the contribution of the internal core to the total moment of inertia, which depends on the infill density factor f_i and its geometry.

On the other hand, beyond the internal heterogeneity introduced by varying material densities, it is also essential to consider the actual geometry of these regions. A key challenge in FFF lies in the discrepancy between the designed and the printed geometry, which stems from the layer-by-layer deposition nature of the process. This discrepancy primarily results from the mismatch between the layer height (t) and the extrusion width (ω), leading to a non-uniform shell thickness, particularly in the top and bottom regions of the specimen.

In horizontal printing, this effect becomes especially pronounced. As illustrated in Figure 2b, the shell no longer forms a continuous and regular ring. Instead, its thickness is significantly reduced at two critical points: the first and the last layers of the cylinder. In these areas, the effective shell thickness is limited to $n{\cdot}t$, which is consistently smaller than $n\omega$ —the theoretical value derived from wall count and extrusion width—. This deviation is not due to a design flaw but is instead an intrinsic feature of the FFF process, resulting from the mechanics of filament stacking.

The slicing software attempts to mitigate this issue by adding extra top and bottom layers, but the compensation is partial at best. Consequently, for accurate mechanical modeling —particularly when calculating the moment of inertia— it is necessary to account for the real printed geometry rather than relying solely on nominal design parameters.

The approach proposed in this work enables a more accurate estimation of the maximum surface stress and, consequently, a more reliable construction of S–N curves for FFF specimens. Four different calculation methods to estimate I, and therefore S_{max}, are evaluated. These methods vary in how they model the shell–infill interface, the assumed geometry of the internal region and the level of simplification. Their predictions are compared to experimental fatigue data to assess the influence of geometric assumptions on life estimation accuracy.

Accepted Manuscript

Method 1 – ISO 1143: Assumes a fully solid circular cross-section, equivalent to applying the ISO 1143:2010 standard [21] without correction.

Method 2 – Infill-Based Method (IB): Studies the section modulus considering only the infill region and neglecting the shell. The effective inertia is scaled according to the infill percentage, but no shell geometry is included.

Method 3 – Dual-Component Method (DC): Models the section as a composite of a solid outer shell and a circular inner core with partial density. The interface is assumed to be circular, and the shell has uniform thickness.

Method 4 – Analytical Geometry-Based Method (AGB): Incorporates a realistic geometric description based on the actual morphology of horizontally printed FFF cylinders. It considers an oval interface between shell and infill and non-uniform shell thickness, identifying the critical section for fatigue failure.

These methods are compared in terms of their predicted stress levels and their influence on the shape and position of the resulting S–N curves. By gradually incorporating the morphological complexity of FFF components, the following analysis aims to provide a more rigorous framework for interpreting rotating bending fatigue results and helps bridge the gap between standardized metallic testing and the reality of polymeric AM parts.

3. Estimation of Section Properties

As discussed in Section 2.3, applying ISO 1143 [21] directly to FFF specimens using Method 1 – ISO 1143 assumes a fully solid circular cross-section. This assumption is only valid for fully dense specimens $f_i = 100\%$ with uniform shell thickness. However, for $f_i < 100\%$, there is a lack of material that reduces the effective moment of inertia of the section. Therefore, this work introduces three alternative analytical approaches to estimate the moment of inertia I (and section modulus W) for rotating bending which are then used to compute $S_{\max}$ through the classical relation used for fatigue life prediction (equation 1).

3.1. Method 2 – IB

This approach considers only the contribution of the infill region, disregarding the structural reinforcement provided by the shell (Figure 5). It assumes that the effect of the shells on section modulus W is negligible, and that I can be calculated considering only the infill.

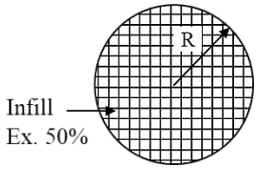

Figure 5. Cross-section representation of the Method 2 – IB specimen, which considers only the infill and excludes the shell by definition

This hypothesis assumes that the lack of infill mass in percentage is equivalent to a proportional loss in inertia, disregarding the existence of the shell. Consequently, the cross-section can be modeled as a solid cylinder, being the moment of inertia (equation 5) and the section modulus (equation 6) obtained according to the ISO 1143 standard and proportionally to the infill factor $f_i \in [0,1]$.

Accepted Manuscript

$$I_{Total}^{M2} = f_i \cdot \frac{\pi}{4}(R^4) \quad \text{Eq. 5}$$

$$W^{M2} = \frac{I_{Total}^{M2}}{R} = \frac{\pi}{4}[f_i \cdot R^3] \quad \text{Eq. 6}$$

As discussed in section 5, this method introduces a correction for the infill density which might be appropriate if the contribution of the shell is negligible with respect to the infill, e.g. in the specimen shown in Figure 3a. However, it underestimates the total stiffness of the cross-section, especially in specimens with a significant number of outer shells, as in the case of the specimen shown in Figure 3b.

3.2. Method 3 – DC

This method models the cross section as two components: (1) a solid outer ring whose thickness corresponds to $n\omega$, and (2) a circular inner core, which is not necessarily solid. As shown in Figure 6, the interface between the infill and the shell is assumed circular and the shell has uniform thickness $R_o - R_i = n \cdot \omega$, where R_o and R_i are the outer and inner radii of the shell respectively.

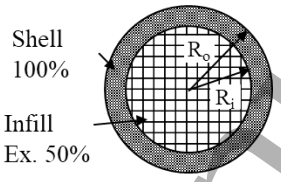

Figure 6. Cross-section representation of the Method 3 – DC specimen, which models the section as two separate parts: a circular outer shell and a central infill

Considering that the infill is circular and the shell forms a solid ring (i.e., with no internal gaps), the moment of inertia and section modulus from equations 7 and 8 were used to calculate the maximum stress S_{max}, respectively. The details of the process to obtain these equations are included in Appendix I.

$$I_{Total}^{M3} = f_i \cdot \frac{\pi}{4}(R_i^4) + \frac{\pi}{4}(R_o^4 - R_i^4) = \frac{\pi}{4}[R_o^4 + (f_i - 1)R_i^4] \quad \text{Eq. 7}$$

$$W^{M3} = \frac{I_{Total}^{M3}}{R_o} = \frac{\pi}{4}[R_o^3 + (f_i - 1)R_i^4/R_o] \quad \text{Eq. 8}$$

This method provides a reasonable approximation of the geometry observed in cylindrical specimens printed vertically, such as those shown in Figure 3b. However, a closer examination to the cross-section of horizontally printed specimens reveals that the interface between the infill and the shell is not circular, and the shell thickness is non-uniform (Figure 4a and 4b). Specimens with this geometry are better represented using Method 4 (AGB).

3.3. Method 4 – AGB

This method incorporates a more realistic geometric description based on the actual morphology of horizontally printed FFF cylinders. It considers an oval interface between shell and infill and non-uniform shell thickness, enabling the identification of the critical section for fatigue failure (Figure 7).

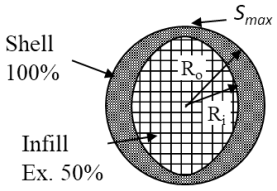

Accepted Manuscript

Figure 7. Cross-section representation of the Method 4 – AGB specimen, which includes a more realistic oval-shaped interface between the infill and the outer shell

Following the procedure introduced in section 2.3 (Equation 4), the analytical expression of the total moment of inertia can be obtained as the sum of the moment of inertia of the infill and the shell respectively. To this regard, the partial moments of inertia are calculated separately as represented in Figure 8.

It must be noted that the cross-section assumed in this method is not axisymmetric, therefore, the total moment of inertia and S_{max} depend on the angular orientation of the specimen within the cross-section plane. In the following calculations, the cross-section is oriented with its minimum shell thickness located at the top and bottom, as shown in Figure 9. Under loading along the y-axis, this orientation results in the lowest moment of inertia and the highest S_{max}, which corresponds to the location where fatigue cracks due to rotating bending typically initiate. Accordingly, the moment of inertia calculations presented below are based on this orientation.

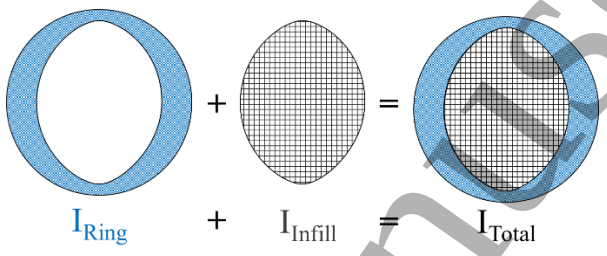

Figure 8. Decomposition of the cross-section used in Method 4 – AGB for inertia calculation. The total moment of inertia is obtained as the sum of two components: the non-uniform outer shell, and the central core. The orientation corresponds to the critical case with minimum shell thickness aligned vertically.

Figure 9a depicts the geometry of the shell over one quarter of the cross section. Due to the characteristics of the printing process, the inner arc of the shell profile (arc *p'q'*) has the same radius as the external arc (arc *pq*) with its center displaced by a distance of $n\omega$ to the left. This detail is essential for accurately determining the moments of inertia of the elements of the section. To compute the moments of inertia of both the ring and the infill, five auxiliary regions (A-E) are defined as illustrated in Figure 9.

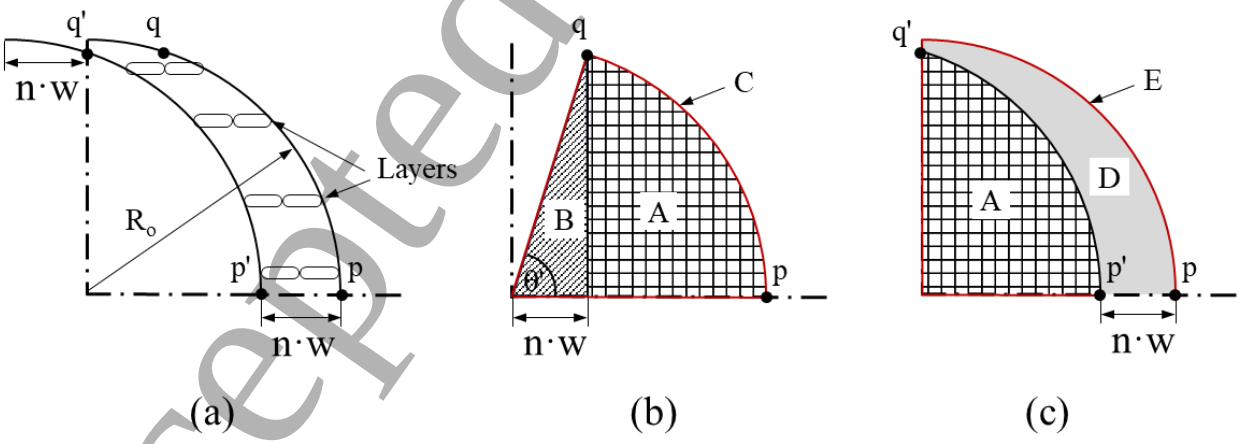

Figure 9. Schematic representation of one-quarter of the cross-section of a horizontally printed specimen. (a) Geometric details of the arcs defining the shell profile. (b) Auxiliary regions used to calculate the moment of inertia of the infill. (c) Auxiliary regions used to calculate the moment of inertia of the shell. Regions A and D correspond to the infill and shell areas, respectively. In horizontally printed specimens, the shell thickness is non-uniform around the perimeter; the minimum shell thickness in the vertical direction defines the critical section that governs the maximum outer-fiber stress under rotating bending.

Accepted Manuscript

The calculation of the moment of inertia begins with the determination of I_x^A, corresponding to auxiliary region A (Figure 9b), which is enclosed between the arc segment pq and the adjacent leg of triangular region B. This term is computed using Equation 9, based on the superposition of the moments of inertia of regions B and C with respect to the x-axis, denoted as I_x^B and I_x^C, respectively.

$$I_x^A = I_x^C - I_x^B \quad \text{Eq. 9}$$

Although the final expression of I_x^A is represented in terms of $n \cdot \omega$, the moment of inertia of region C with respect to the x-axis is obtained through the standard formula for second moment of area of circular sector about the x-axis, as shown in Equation 10. The integration limits are defined over the radial domain $R \in [0, R_o]$ and the angular sector $\theta \in [0, \theta']$ which is defined in Figure 9b.

$$I_x^C(\theta') = \int_0^{\theta'} \int_0^{R_o} (R^3 sin^2\theta) dR d\theta = \frac{R_o^4}{8}\left[\theta' - \frac{sin(2\theta')}{2}\right] \quad \text{Eq. 10}$$

The moment of inertia of region B (I_x^B) corresponds to that of a right triangle with one leg aligned along the x-axis, as shown in Equation 11. In this expression, R_o denotes the outer radius of the specimen cross-section, n is the number of shell layers, and ω is the extrusion width of each layer. For consistency with the formulation of I_x^C in Equation 12 and to simplify the analytical expression of I_x^A, the actual expression of I_x^B has also been reformulated in terms of θ', as given in equation 13.

$$I_x^B(\,\mathrm{n}, \omega) = \frac{bh^3}{12} = \frac{n\omega}{12}\left(\sqrt{R_o^2 - (n \cdot \omega)^2}\right)^3 \quad \text{Eq. 11}$$

$$n \cdot \omega = R_o \cdot cos(\theta') \quad \text{Eq. 12}$$

$$I_x^B(\theta') = \frac{R_o^4}{12} cos(\theta') sin^3(\theta') \quad \text{Eq. 13}$$

Thus, the moment of inertia of region A (I_x^A) expressed in terms of θ' is given by the following equation:

$$I_x^A(\theta') = \frac{R_o^4}{16}\left(2\theta' - sin(2\theta')\right) - \frac{R_o^4}{12}\cos(\theta') sin^3(\theta') \quad \text{Eq. 14}$$

Now, according to Figure 9b and considering that the displacement of region A along the x-axis does not affect its moment of inertia with respect to that axis, the moment of inertia of region D can be calculated as:

$$I_x^D = I_x^E - I_x^A \quad \text{Eq. 15}$$

The expression for the moment of inertia of region E has been calculated using the same approach employed for I_x^A, with the angular integration limits set to the interval $\theta = [0, \pi/2]$ in radians, as shown in Equation 16. Subsequently, the moment of inertia of the shell with respect to the x-axis I_x^D, is obtained by combining the contributions of the relevant regions, as defined in Equation 17.

$$I_x^E = \frac{\pi}{16} R_o^4 \quad \text{Eq. 16}$$

$$I_x^D(\theta') = \frac{R_o^4}{16}\left(\pi - 2\theta' + sin(2\theta')\right) + \frac{R_o^4}{12}\cos(\theta') sin^3(\theta') \quad \text{Eq. 17}$$

Because the derivation to obtain I_x^D and I_x^A (Equation 17) is performed over one quarter of the cross-section, the full-section inertia is obtained by symmetry (multiplication by 4). The infill contribution is approximated by scaling the solid-core inertia by the infill fraction f_i (with $f_i = 1$ representing a fully solid core). Using Equation 17, the inertias of the shell (I_{Shell}), the infill (I_{Infill}) and the sum of them (I_{Total}), as represented in Figure 8, can be calculated as follows:

Accepted Manuscript

$$I_{Shell}(\theta') = 4 \cdot I_x^D = \frac{R_o^4}{4}\left(\pi - 2\theta' + sin(2\theta')\right) + \frac{R_o^4}{3}\cos(\theta')sin^3(\theta') \quad \text{Eq. 18}$$

$$I_{Infill}(\theta') = 4 \cdot f_i \cdot I_x^A = f_i \cdot \left[\frac{R_o^4}{4}\left(2\theta' - sin(2\theta')\right) - \frac{R_o^4}{3}\cos(\theta')sin^3(\theta')\right] \quad \text{Eq. 19}$$

$$I_{Total}(\theta') = I_{Shell}(\theta') + I_{Infill}(\theta') = \frac{R_o^4}{4}\left[\pi + (1 - f_i)\left(-2\theta' + sin(2\theta') + \frac{4}{3}\cos(\theta')sin^3(\theta')\right)\right] \quad \text{Eq. 20}$$

As commented before, expressing the inertia of the different parts in terms of the variable θ' has simplified the calculation process. However, it is more intuitive to express them using the variables (n, ω), i.e. the number of shells and the layer width respectively, as far as these are the real design parameters when manufacturing parts by FFF. To express the result in terms of design parameters, θ' is eliminated from Equations 18-20 using Equation 12, yielding closed-form expressions (Equations 21-23) for moment of inertia of the shell I_{Shell}, the infill I_{Infill}, and the total section $I_{Total} = I_{Shell} + I_{Infill}$, respectively, as functions of (n, ω) and f_i.

$$I_{Shell}(n, \omega) = \frac{R_o^4}{4}\left(\pi - 2\,\text{acos}\left(\frac{n\omega}{R_o}\right) + sin\left(2\,\text{acos}\left(\frac{n\omega}{R_o}\right)\right)\right) + \frac{n\omega}{3}\left({R_o}^2 - (n\omega)^2\right)^{3/2} \quad \text{Eq. 21}$$

$$I_{Infill}(n, \omega) = f_i \cdot \left[\frac{R_o^4}{4}\left(2\,\text{acos}\left(\frac{n\omega}{R_o}\right) - sin\left(2\,\text{acos}\left(\frac{n\omega}{R_o}\right)\right)\right) - \frac{n\omega}{3}\left({R_o}^2 - (n\omega)^2\right)^{3/2}\right] \quad \text{Eq. 22}$$

$$I_{Total}(n, \omega) = \frac{R_o^4}{4}\left[\pi + (1 - f_i) \cdot \left(sin\left(2\,\text{acos}\left(\frac{n\omega}{R_o}\right)\right) - 2\,\text{acos}\left(\frac{n\omega}{R_o}\right)\right)\right] + (1 - f_i)\frac{n\omega}{3}\left({R_o}^2 - (n\omega)^2\right)^{3/2} \quad \text{Eq. 23}$$

Equation 23 provides the final analytical estimate of the total moment of inertia for Method 4, which is subsequently divided by R_o to compute the section modulus represented by Equation 24.

$$W^{M4}(n, \omega) = \frac{R_o^3}{4}\left[\pi + (1 - f_i) \cdot \left(sin\left(2\,\text{acos}\left(\frac{n\omega}{R_o}\right)\right) - 2\,\text{acos}\left(\frac{n\omega}{R_o}\right)\right)\right] + (1 - f_i)\frac{n\omega}{3R_o}\left({R_o}^2 - (n\omega)^2\right)^{3/2} \quad \text{Eq. 24}$$

Considering Equation 23 and Equation 1 the maximum stress (S_{max}) can be obtained. This method can be considered more accurate in the calculation of horizontally printed cylinders, since it uses an analytical expression of the exact cross-section geometry.

4. Comparative study of the proposed methods

To evaluate the mechanical implications of the different modeling approaches introduced in Sections 3.1 to 3.3, this section presents a comparative study based on two key parameters: the moment of inertia I_x and the maximum stress S_{max}. These parameters are discussed separately to isolate the influence of geometry (through I_x) and to assess the fatigue-relevant stress response (through S_{max}) under a representative loading condition.

4.1. Effect of Infill and Shell Thickness on the Moment of Inertia I_x

In cylindrical components produced by FFF, I_x is primarily governed by two geometric factors: the infill density f_i and the shell thickness $n{\cdot}\omega$.

At constant shell thickness, I_x increases with the infill density, as illustrated in Figure 10a. Method 1 (ISO) predicts a constant inertia regardless of the infill or shell configuration. While this method is only valid for 100% solid specimens, it has been included in this analysis as a reference baseline.

Among the other approaches, **Method 2 (IB)** — which excludes the shell contribution but includes the effect of the infill density — is the most sensitive to changes in fi. **Method 3 (DC)**, which models the shell as a uniform

Accepted Manuscript

ring, shows the least sensitivity, as it underestimates the impact of the variable infill. **Method 4 (AGB)**, which incorporates both the infill and a realistic representation of the shell geometry, consistently yields I_x values between those predicted by Methods 2 and 3 for all infill levels. This behavior highlights the structural reinforcement provided by the outer shell—even in small thicknesses—and reinforces the importance of accurately modeling its geometry to obtain reliable stiffness estimations.

On the other hand, at constant infill density, the evolution of the moment of inertia I_x with increasing shell thickness $n{\cdot}\omega$ highlights the differences between the structural assumptions of each method.

As shown in Figure 10b, although I_x is constant for Method 1 and Method 2, the value obtained from Method 2 is significantly lower since it completely neglects the shell contribution. This simplification leads to a clear underestimation of the real structural stiffness, especially in specimens with multiple outer contours.

The two remaining methods, which incorporate the shell in their formulations, show an increasing trend of I_x with respect to shell thickness. Method 3 (DC) assumes a shell with idealized ring geometry, which results in a rise of inertia as material is added further from the neutral axis. However, this idealization tends to overpredict the stiffness gain, especially in the case of horizontally printed specimens, where the actual shell profile deviates from a perfect circular ring.

Method 4 (AGB), which introduces a more realistic geometric representation of the shell, including its non-uniform thickness and oval interface with the infill, yields a more gradual and physically consistent increase in inertia. Its curve remains between those predicted by Methods 2 and 3 throughout the range of shell thickness values, accurately reflecting the partial reinforcement provided by the shell under realistic FFF conditions.

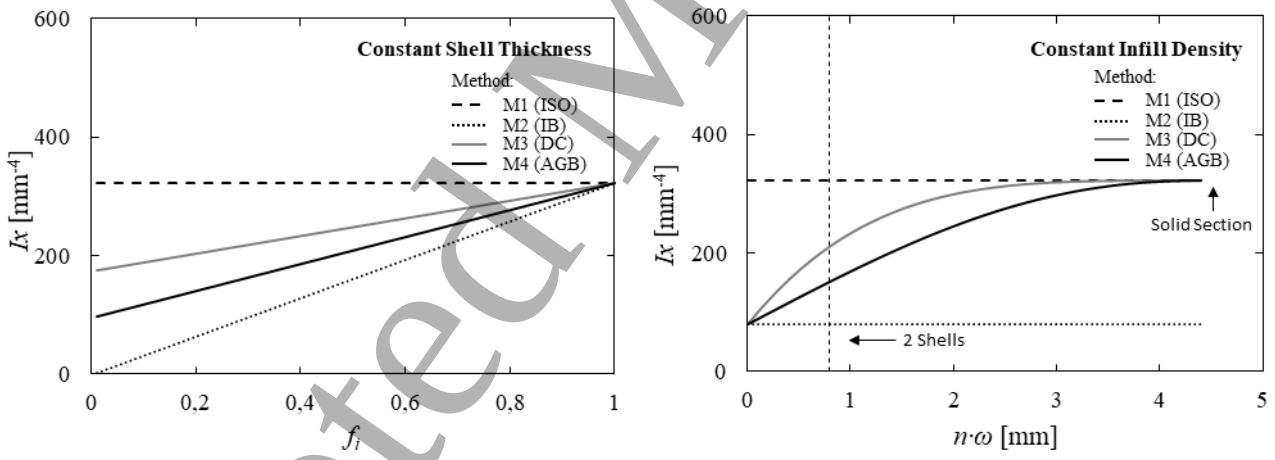

Figure 10. Inertia evolution with the infill density (a) and the shell thickness (b). Variations in shell thickness, particularly the minimum thickness in horizontally printed sections, can dominate the effective section properties and thus the stress level used for fatigue assessment.

4.2 Stress-Based Comparison Under Experimental Bending Conditions

While the moment of inertia offers valuable insights into the structural stiffness of the specimen, fatigue failure is ultimately governed by the maximum surface stress developed under bending loads. To assess the relevance of each method in practical fatigue scenarios, the estimated surface stress S_{max} has been computed under a fixed bending moment representative of the experimental setup: $M = F \cdot \mathrm{x} = 300$ N·mm.

Accepted Manuscript

Figure 11a to c show the evolution of S_{max} as a function of shell thickness $n{\cdot}\omega$ for different infill percentages, according to Methods 2, 3, and 4. For reference, the result of Method 1 (ISO), which corresponds to the stress in a fully solid section, is represented as a horizontal line in all cases. Additionally, a vertical dashed line is included in each figure to indicate the case of two shell layers of 0.4 mm each (i.e., $n{\cdot}\omega$ = 0.8 mm). This configuration has been selected as a representative condition and is further analyzed in Section 5.

In Method 2 (Figure 11a), the absence of shell contribution leads to a strong dependency of S_{max} on the infill density. At low shell thickness and reduced infill percentages, the predicted surface stress increases significantly, reaching values far beyond those expected in real specimens. This makes the method overly conservative and unrealistic for typical FFF configurations.

In contrast, **Method 3** (Figure 11b) introduces a more moderate behavior. By accounting for a uniform circular shell, the method reduces the surface stress as the shell thickness increases. However, the assumption of ideal ring geometry leads to a steep decline of S_{max} at low shell thickness values, overestimating the mechanical benefit of the shell, particularly when the material distribution is not uniform. Despite this limitation, the simplified geometry used in Method 3 makes it especially suitable for vertically printed specimens, where the shell tends to be more regular and concentric, aligning well with the assumptions of the method.

Method 4 (Figure 11c), which incorporates the actual non-uniform geometry of horizontally printed shells, provides the smoothest and most realistic evolution of S_{max}. The stress values decrease progressively with increasing shell thickness, and the sensitivity to infill density is also reduced compared to Method 2. This behavior aligns with the physical mechanisms of fatigue failure, which tend to initiate in regions of minimal shell thickness—well captured in this formulation. Although this method offers the most accurate representation for horizontally printed specimens, its detailed geometric treatment may be less critical for vertically printed parts, where simpler assumptions such as those in Method 3 remain valid and effective.

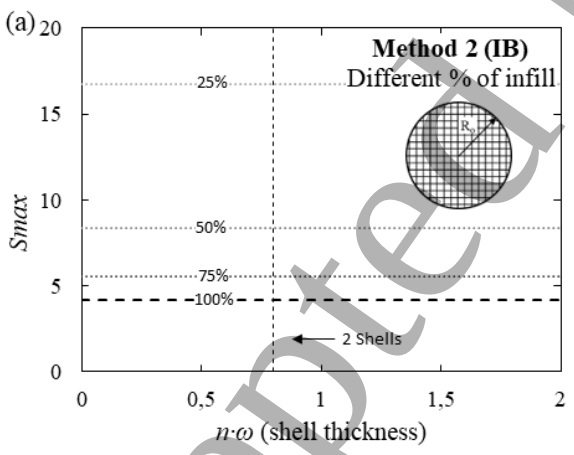

(a)

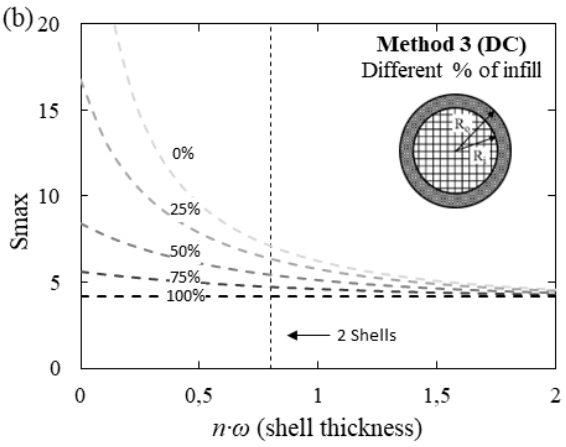

(b)

Accepted Manuscript

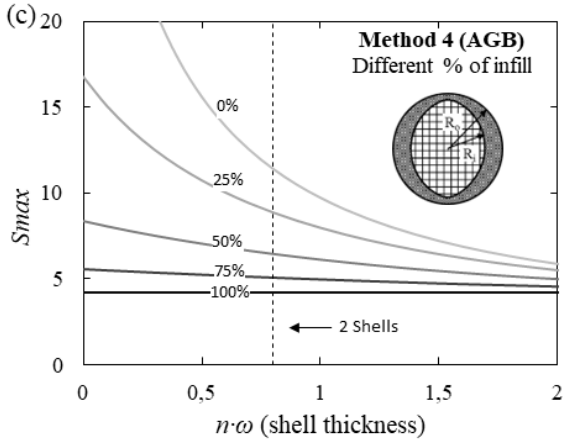

(c)

Figure 11. Estimated maximum surface stress S_{max} as a function of shell thickness $n \cdot \omega$ for different infill percentages using (a) Method 2 (IB), (b) Method 3 (DC), and (c) Method 4 (AGB). The vertical dashed line corresponds to the representative case of two shell layers of 0.4 mm each ($n \cdot \omega$ = 0.8 mm). The strong sensitivity to shell thickness reflects its direct effect on the section modulus; in horizontally printed specimens, non-uniform shell thickness therefore governs the critical stress and the expected fatigue-failure location.

5. Experimental Setup for fatigue testing

The specimens used in this study were designed to be geometrically compatible with the ISO 1143 standard [21]. Each specimen includes a central gauge section with a reduced diameter, which is flanked by two larger diameter ends to allow proper clamping in the fatigue testing machine. The specimen measurements and representative printed samples are shown in Figure 12. The specimens were manufactured using a Raise3D E2 printer with fused filament fabrication (FFF) technology. All samples were printed using PLA under controlled conditions to ensure repeatability. The process parameters (layer height (t), extrusion temperature (T), bed temperature (T_b) and printing speed (v)) were kept constant to ensure repeatability. The percentage of infill changes between 100 and 25%. This allows obtaining different stress conditions in different specimens for a unique loading condition (1 kgf at 30 mm from the critical section) and makes it possible to obtain the Wöhler curves [24]. Table 1 summarizes the main printing parameters used in this study.

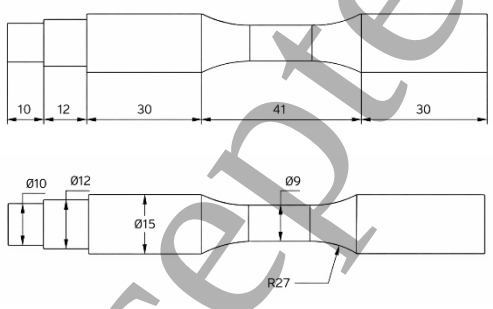

(a)

(b)

Figure 12. Rotating bending fatigue specimens: (a) specimen geometry and dimensions according to ISO 1143:2010; (b) set of horizontally printed PLA specimens prior to raft removal.

Accepted Manuscript

t [mm]	T [ºC]	v [mm/s]	f_i [%]	Pattern	T_b [ºC]	Shells	Shell Thick. [mm]
0.2	215	40	100 - 75 - 50 - 25	Grid	55	2	0.8 (0.4 x 2)
0.2	215	40	100 - 75 - 50 - 25	Honeycomb	55	2	0.8 (0.4 x 2)

Table 1. Printing parameters used for specimen fabrication.

Two printing orientations were considered to analyze the different distributions of material across the specimen section described in section 3. Using the vertical orientation (Figure 3), the cylindrical axis is aligned with the printer's Z-axis. In this case, the printed layers are deposited perpendicular to the direction of the applied stress. This configuration yields a relatively uniform and concentric shell, and the shell-infill interface approximates a circular profile. On the other hand, in the horizontal orientation (Figure 4) the cylindrical axis lies in the XY-plane. Due to the nature of layer-by-layer deposition, this configuration results in the oval cross-sectional shape with non-uniform shell thickness. These differences in geometry and material distribution are critical when estimating the mechanical response of FFF specimens under bending fatigue. As discussed in Section 3, the standard assumptions of a fully solid, homogeneous cross-section are not valid for such cases. Therefore, an accurate estimation of the moment of inertia and resulting stress requires the use of geometry-aware methods, especially for specimens printed horizontally.

The fatigue testing experiments were carried out using a custom-built rotating bending machine (Figure 13). The equipment has been routinely used in our laboratory, and its measurement reliability is supported by prior peer reviewed studies and benchmark tests on metallic alloys showing good agreement with literature data [22,25–28]. The test rig applies a constant bending moment to the specimen while it rotates around its longitudinal axis at a controlled speed. The configuration reproduces fully reversed loading conditions (stress ratio R = –1), in line with the ISO 1143 standard [21].

The machine applies the load through a cantilevered system using adjustable weights positioned at a known distance from the specimen's central axis. By varying the applied mass or specimen infill percentage, different bending moments were generated to explore fatigue behavior at multiple stress levels. The maximum surface stress for each configuration was estimated using the geometric models presented in Section 3, incorporating the real cross-sectional properties of each specimen. The resulting stress values were used to construct the corresponding S–N curves (Wöhler curves) [24], which relate the maximum surface stress to the number of cycles to failure. These curves allow a direct comparison between the predicted and experimental fatigue performance of the printed specimens. Fatigue life was determined by the number of cycles to failure (N) for each specimen. To ensure reliability, a minimum of five specimens per infill condition and pattern were tested, allowing statistical analysis and determination of fatigue life variability. The printing and fatigue testing conditions were selected based on preliminary tests [22,24,29–31] and existing literature [32–35]

Accepted Manuscript

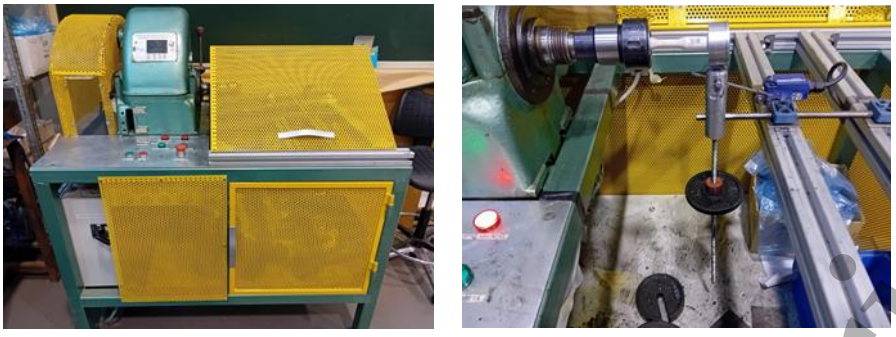

(a) (b)

Figure 13. Custom-built rotating bending machine (a) and test specimen in the test position (b)

The maximum surface stress for each configuration was estimated using the geometric models presented in Section 3, incorporating the real cross-sectional properties of each specimen. The resulting stress values were used to construct the corresponding S–N curves. These curves allow a direct comparison of the different methods to assess their performance in predicting fatigue life. The fatigue test details are provided in Table 2.

	Mat.	Print. Dir.	Load [kgf]	Rotational speed [rev/min]	Frequency [Hz]
Bermudo et al. [24]	FR PLA	Hor.	0.75, 0.9, 1, 1.1	1800	30
This study	PLA	Hor.	1	1800	30

Table 2. Summary of fatigue test data of the different specimens analyzed

6. Results and discussion

This section examines how different estimation methods for the moment of inertia I influence the interpretation of rotating bending fatigue data in FFF specimens. First, previously published experimental results are reanalyzed using methods M2–M4 to assess how the estimated stress changes for a given number of cycles to failure. Then, fatigue life is predicted for PLA specimens under constant bending moment, considering different cross-sectional geometries associated with varying infill densities. Finally, fatigue data from different studies are compared before and after applying the method that best represents the actual geometry of the specimens, in order to evaluate its effect on the consistency and comparability of S–N curves.

6.1. Reinterpretation of Experimental Fatigue Data

Although the number of studies focused on rotating bending fatigue of FFF-manufactured polymers is limited, most of them follow a common approach to estimate the stress amplitude. Specifically, they adopt the formulation of ISO 1143—originally developed for homogeneous, fully solid metallic specimens. This method, referred to as Method 1 (ISO) in this work, neglects the contribution of the outer shell and the non-uniform, anisotropic geometry characteristic of FFF components.

To assess the influence of this simplification, the present study reanalyzes selected fatigue data from the literature using the moment of inertia estimation methods introduced in Section 3. In particular, the original values—typically computed under the assumptions of Method 1—are recalculated using the geometry-aware methods: M2 Infill-Based (IB), M3 Dual-Component (DC), and M4 Analytical Geometry-Based (AGB). This reinterpretation enables a consistent comparison of fatigue life predictions across different studies. It is

Accepted Manuscript

important to note that this procedure constitutes an indirect validation of the proposed methods to estimate the moment of inertia and the resulting stress levels. Rather than measuring stresses or using numerical simulations, the methods are assessed by their ability to rationalize and align existing experimental S–N curves through geometry-aware stress correction. While this approach does not confirm the absolute accuracy of each method, it provides strong evidence that incorporating realistic cross-sectional morphology improves the consistency and interpretability of fatigue life data across multiple studies.

The recalculation procedure involves two steps. First, the original stress values are reversed to obtain the applied bending moment for each data point. This is done by reconstructing the section modulus based on the method originally used (e.g., Equation 2 for M1) and applying Equation 1 using the specimen geometry. Then, the moment is used to recalculate using the section modulus of the new method: Equation 6 for M2, Equation 8 for M3, and Equation 24 for M4. These corrected stress values, which reflect a more realistic cross-sectional geometry, are then used to reconstruct the corresponding S–N curves.

Figure 14 shows a set of S–N curves obtained from the experimental studies by Bermudo Gamboa et al. [24] and Parast et al. [35] on horizontally printed PLA specimens, with the printing parameters summarized in Table 3. In both cases, the original analysis was based on the M1 (ISO) method, which assumes a fully solid circular cross-section and does not account for the internal infill pattern or the outer shell. This leads to an underestimation of the stress for a given load, and thus to an overestimation of the fatigue life.

	Mat.	Print. Dir.	Orig. Meth.	New Meth.	Diameter [mm]	Infill [%]	Shell Thick. [mm]
Bermudo et al. [24]	FR PLA	Hor.	M1	M4	6	50	1.6
Parast et al. [35]	PLA	Hor.	M1	M4	6	75	1.5
Azadi et al. [23]	PLA	Vert.	M1	M4	6	50	0.8
Azadi et al. [23]	PLA	Vert.	M1	M3	6	50	0.8
This study	PLA	Hor.	-	M4	9	25–100	0.8

Table 3. Summary of data of the different rotating bending fatigue specimens analyzed in this section, and the original and proposed method for calculation of section modulus.

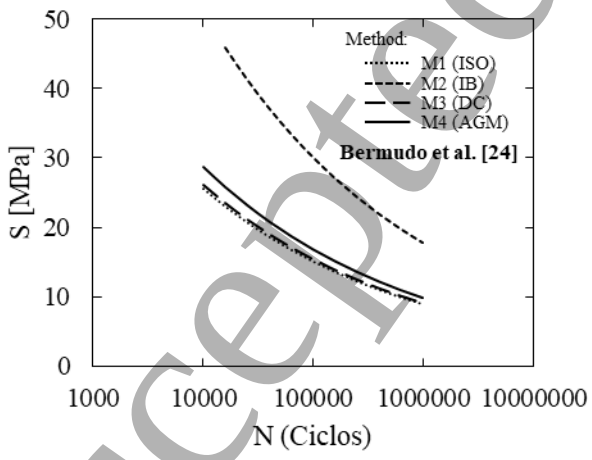

(a)

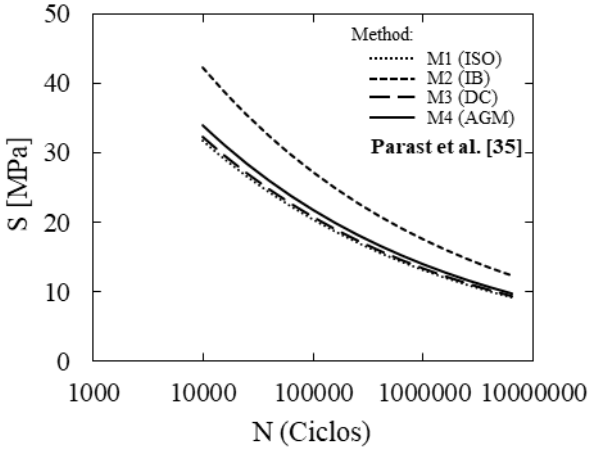

(b)

Accepted Manuscript

Figure 14. Reinterpretation of fatigue life data using different methods for calculation of the section modulus. (a) Fatigue results for carbon fiber-reinforced PLA from Bermudo et al. [24] and (b) fatigue life results for PLA from Parast et al. [35]. The results correspond to specimens printed horizontally.

When the same experimental data are reprocessed using geometry-based methods accounting for shell and infill structure, the estimated stress increases due to the reduced effective section of the printed specimens. In this case, since the specimens were printed horizontally, the most appropriate method is M4 (AGB), which incorporates both the shell and core morphology. This leads to a more realistic estimation of the number of cycles to failure for a given applied stress. As shown in Figure 14, the M1 (ISO) method underestimates the stress amplitude S_{max}, while the M4 (AGB) method—by capturing the actual cross-sectional geometry—predicts a larger number of cycles.

Notably, the curves corresponding to M1 (ISO) and M3 (DC) are relatively close. In vertically printed specimens with a particularly thick outer shell or high infill density, the difference between both methods may become negligible, and M1 may yield similar predictions to M3 or even M4.

To further generalize the observations, **Figure 15** presents the reinterpretation of fatigue data from an additional source: Azadi et al. [25], who tested PLA specimens manufactured by FFF in both horizontal and vertical orientations (see Table 3). In both cases, the original S_{max} values were obtained using a methodology consistent with Method 1 (ISO). These values have now been recalculated using all four methods, M1 through M4.

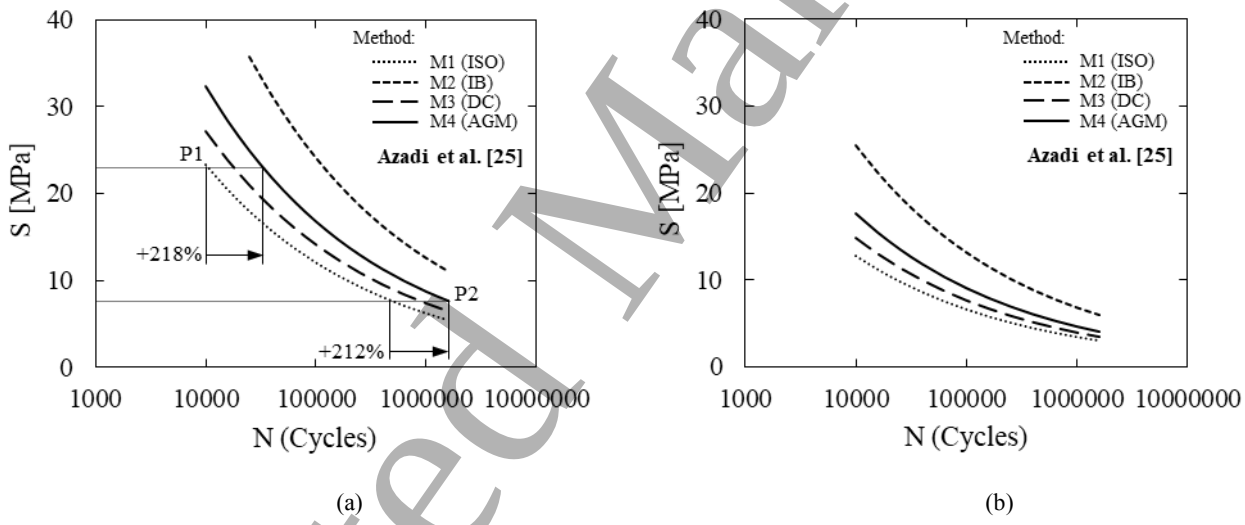

Figure 15. Rotating bending fatigue results obtained from Azadi et al. [25] for PLA printed by FFF (a) horizontally and (b) vertically, respectively.

As shown in Figure 15, the original curves presented in both studies move upward when the stress values are recalculated with the proposed methods. An upward shift of the curve indicates a longer fatigue life. Among the methods, Method 2 (IB)—which neglects the shell contribution—predicts the longest fatigue life due to the highest estimated stresses. This is followed by Method 4 (AGB), which accounts for the actual shell–infill geometry typical of horizontally printed parts, and finally by Method 3 (DC), which assumes a simplified shell with uniform ring shape.

As previously discussed, the most appropriate method depends on the build orientation of the specimen. For horizontally printed parts, the M4 (AGB) method provides the best representation of the actual cross-sectional geometry. Figure 15a illustrates the difference in predicted number of cycles between the original curve from

Accepted Manuscript

Azadi et al. [25] and the recalculated curve using M4. For two representative points on the curve, the revised prediction shows an increase in fatigue life of over 200% compared to the original estimation.

Figure 15b shows the application of the same methods to the vertically printed specimens. In this case, the most appropriate method is M3 (DC), as it more closely matches the typical shell configuration observed in vertically printed specimens. Here too, the corrected curve indicates an increase in predicted fatigue life relative to the original.

To summarize these results, Table 4 compares the original curves with those obtained using the most appropriate method for each configuration. It includes the absolute and relative increase in the number of cycles at both ends of the curve, as illustrated in Figure 15a. Even in the most conservative case, the number of cycles increases by 39%, reaching up to 212% in the case of horizontally printed PLA from Azadi et al. [25].

	S_f – M1 [MPa]	S_f – M4 [MPa]	b	ΔN-P1 [Cycles]	ΔN-P2 [Cycles]	ΔN-P1 [%]	ΔN-P2 [%]
Bermudo et al. [24]	212.5	238.46	-0.230	14800	383100	48 (+)	62 (+)
Parast et al. [35]	186.0	198.6	-0.192	4100	1766200	41 (+)	39 (+)
Azadi et al. [25] Hor.	321.27	447.21	-0.285	21800	1077400	218 (+)	212 (+)
Azadi et al. [25] Vert.	180.3	210.7	-0.288	7200	706300	72 (+)	80 (+)

Table 4. Rotating bending fatigue data from previous studies and corresponding recalculated values obtained using the proposed methods for estimating the maximum stress amplitude. The last row corresponds to vertically printed PLA specimens. The S–N data were fitted using $S = S_f\, N^b$, where S_f is the fatigue strength coefficient and b is the fatigue exponent.

These results highlight the importance of selecting a stress estimation method that accurately reflects the actual cross-sectional geometry of the specimens. This is particularly critical in FFF-manufactured parts, where the internal structure can be configured with different infill patterns and shell thicknesses. The analysis presented in this study has emphasized the differences between the available methods and identified the most suitable approach for each case: Method 3 (DC) for vertically printed specimens, and Method 4 (AGB) for horizontally printed ones.

6.2. Estimation of fatigue life varying the infill density

S–N curves in rotating bending fatigue are typically obtained by performing tests under different stress levels. Each point on the curve corresponds to a different applied bending moment. However, as proposed in this study, it is also possible to vary the stress amplitude S_{max} by changing the cross-sectional properties of the specimen. While this approach is uncommon in metals, it becomes feasible in FFF-manufactured parts by modifying the infill density or shell thickness. This feature enables an alternative method for constructing fatigue life curves: varying the section geometry while applying a constant external load.

This section presents an alternative approach for estimating fatigue life in rotating bending, based on varying the infill percentage. Horizontally printed PLA specimens were tested under constant loading conditions, as described in Section 5. Two different infill types—honeycomb and grid—were used to evaluate the influence of internal geometry on fatigue performance. The full set of manufacturing parameters is detailed in Table 1.

Figure 16 shows the S–N curves obtained for both infill types, generated by applying a single load level while varying the infill percentage. It represents the discrete cycles-to-failure data for each condition (grid and

Accepted Manuscript

honeycomb), which constitute the basis for the fitted S–N curves; quantitative scatter of replicate tests is reported in the corresponding load or bending moment versus cycles to failure plots provided in the referenced studies.

Although all other printing parameters were kept constant, the infill pattern was found to significantly affect fatigue life. In this case, honeycomb structures exhibited lower resistance to rotating bending fatigue than grid infill. This difference may be attributed to the distinct stress concentration associated with each pattern. Grid structures provide more continuous and orthogonal paths for load transmission, which may improve stiffness and delay crack initiation. In contrast, honeycomb patterns, despite offering high isotropic stiffness under static loads, can introduce local stress concentrations at the nodal junctions and curved struts, which may accelerate fatigue damage under cyclic bending. Further investigation would be required to isolate the microstructural mechanisms responsible for this behavior. However, the difference between the two patterns is notably smaller in the low-cycle region (e.g., around N = 10^4 cycles), showing that at higher load levels, the dominant factor influencing fatigue life appears to be the infill density rather than the infill pattern itself.

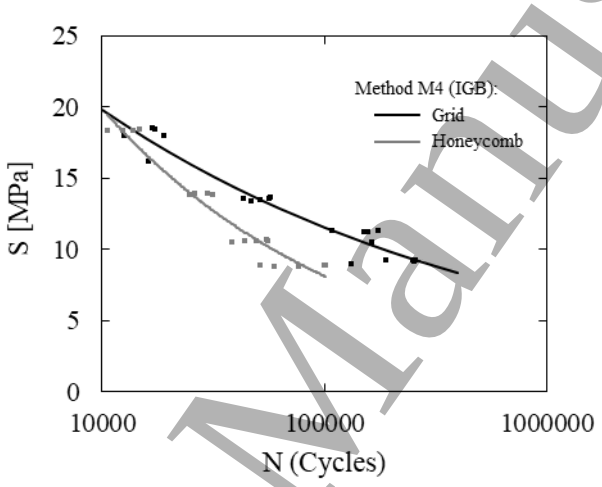

Figure 16. Rotating bending fatigue life (S–N) curves for PLA specimens manufactured by FFF using two different infill patterns (grid and honeycomb). Curves were generated by varying the infill density under constant applied load.

6.3. Geometry-Independent Stress Estimation

Components produced by fused filament fabrication (FFF) exhibit fatigue performance that is highly sensitive to printing parameters, making fatigue life strongly dependent on manufacturing conditions. As a result, FFF specimens typically show large variability in fatigue behavior, with broad statistical scatter even under controlled testing. Small differences in filament deposition, interlayer bonding, or geometric irregularities can significantly affect crack initiation and propagation, leading to inconsistent fatigue lives among nominally identical samples.

Despite this complexity, achieving a geometry-independent characterization of fatigue behavior remains a desirable goal—particularly if fatigue life data obtained from test specimens are to be extrapolated to real parts. This is only possible if the stress used in fatigue life estimation reflects the actual load-bearing geometry of the section. Methods such as M3 (DC) and M4 (AGB), which account for the true shell–core structure of printed sections, allow for obtaining S–N curves that are less dependent on specimen geometry.

Accepted Manuscript

To explore this, previously published fatigue data for polylactic acid (PLA) were reprocessed using the proposed methods. The original curves, calculated using the ISO 1143 formulation (M1), are shown in Figure 17a. These data were recalculated using M3 or M4—depending on the printing orientation—to obtain updated stress values, leading to corrected S–N curves shown in Figure 17b. In addition, new data obtained in this study for grid and honeycomb infill patterns under constant loading are included in the comparison.

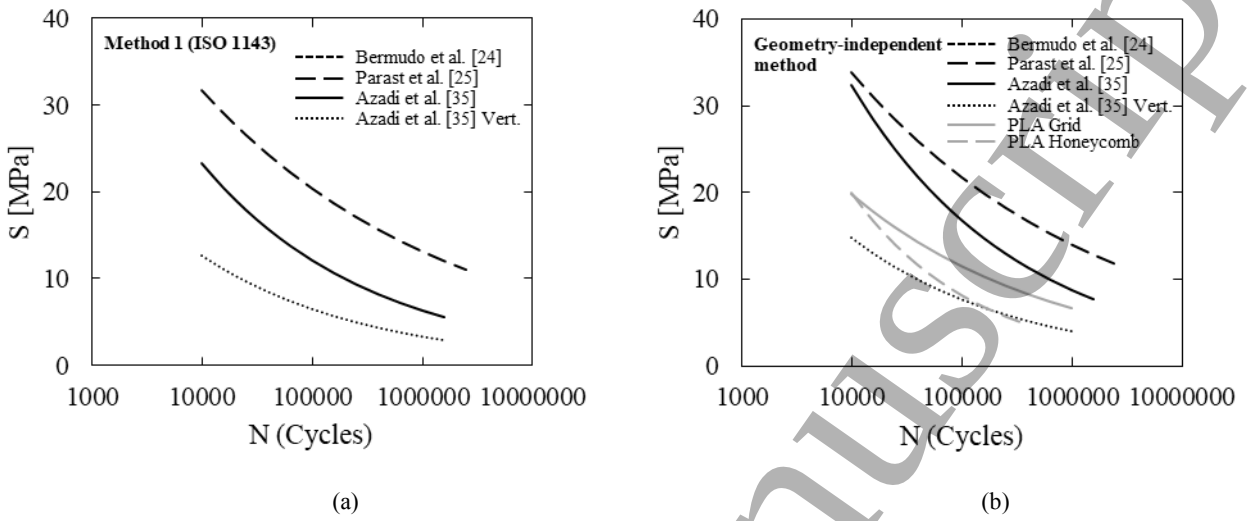

(a) (b)

Figure 17. Rotating bending fatigue S–N curves for PLA from different studies, obtained using (a) the ISO 1143 standard and (b) the method that best represents the actual cross-sectional geometry.

As shown in Section 6.1, geometry-aware section properties increase the estimated stress for a given load, which affects the location of the S–N curves. Ideally, if all other parameters were held constant, fatigue curves from different studies should align closely. However, even after correcting for geometric differences, Figure 17 still reveals noticeable discrepancies between the literature data and the results obtained in this study. To complement this geometry-based comparison, representative fracture-surface observations are shown in Figure 18 to support the assumed critical region in horizontally printed specimens.

Figure 18 presents the fracture surface of a horizontally printed specimen manufactured with 80% infill, including an optical image and an SEM micrograph of the same section. In the optical image, classical metallic fatigue beach marks are not clearly distinguishable because the layer-by-layer morphology inherent to FFF tends to mask concentric propagation features. Nevertheless, the upper third of the section exhibits a comparatively brighter and smoother region, consistent with crack initiation and early stable propagation, whereas the remaining surface appears more irregular. A darker feature near the lower edge is associated with the final fast fracture. This interpretation is clearer in the SEM image, where a relatively smooth region is observed at the top of the section followed by a markedly rougher morphology at the bottom, characteristic of the final catastrophic rupture.

Accepted Manuscript

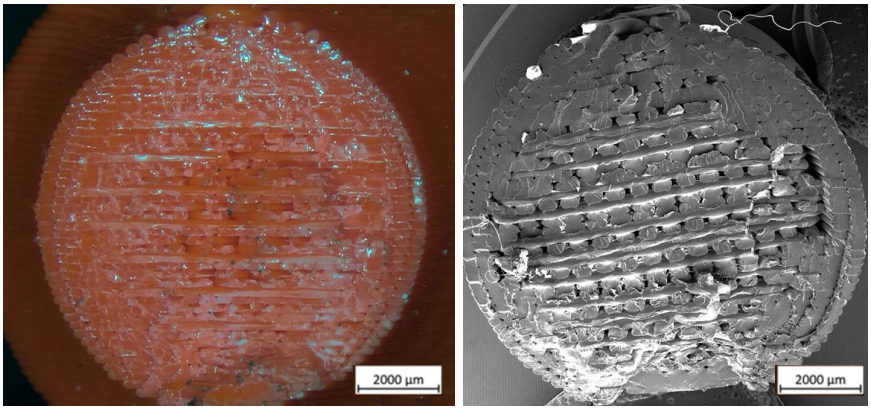

(a) (b)

Figure 18. Fracture surface of a horizontally printed PLA specimen tested under rotating bending fatigue (80% infill): (a) optical image of the section; (b) SEM image of the same section.

(**c**) 2 shells, 0.3 mm layer height, 50% infill (**d**) crack initiation and early propagation region located at the minimum shell thickness zone **for a specimen horizontally printed with 100% infill**.

Nevertheless, although all data refer to PLA, the FFF process involves many printing parameters that influence fatigue performance. The remaining differences likely reflect variability in those parameters. In fact, the new results show that the type of infill alone—regardless of density or load—has a measurable influence on fatigue life, as seen in the separation between the grid and honeycomb curves. Therefore, while applying geometry-based stress estimation methods represents a significant step toward a more universal fatigue characterization of FFF materials, further investigation is needed to understand and control the effects of other processing parameters.

In this context, the agreement between corrected curves may be influenced by uncertainties in the effective load transfer between shell and infill, interlayer bonding quality, and the effective stiffness contribution of the infill, which can vary with defects, porosity, and process-induced variability. In addition, the infill architecture produces a directional (anisotropic) core response, so changes in pattern and density may introduce scatter that is not captured by section-property estimation alone. The degree of shell–infill bonding is also expected to depend on the characteristic length scale of the pattern (and thus on f_i), since finer patterns increase interfacial contact area and may promote more efficient load transfer than coarser patterns.

These considerations are particularly relevant for Methods 2–4, where the infill contribution is scaled using the infill factor f_i. This proportional scaling is an approximation, because the infill is not distributed uniformly over the cross-section but concentrated along the pattern paths. As a result, at low f_i the load-bearing contribution of the core may produce more scatter, whereas the approximation is expected to improve as infill density increases and the characteristic feature size decreases. Moreover, different infill patterns can exhibit different effective stiffness and anisotropy; therefore, for a given f_i, grid and honeycomb infill may not contribute equally to the bending response. Further work should quantify these effects by linking geometry-aware section reconstruction with independent characterization of effective infill stiffness and shell–infill bonding.

Accepted Manuscript

Although this study focuses on PLA and cylindrical specimens, the underlying methodology does not depend on the material in the sense that stress estimation follows from the section properties. Therefore, the AGB framework could be extended to other thermoplastics (e.g., ABS, PETG) and to fiber-reinforced filaments, provided that the effective contribution of the core and the shell–infill load transfer are re-evaluated for the corresponding material system and printing conditions. Extension to non-cylindrical cross-sections is also feasible by applying the same principle at the expected critical section and computing section properties with respect to the actual bending direction; in many practical cases this may require numerical section integration or finite element modeling when a closed-form expression is not available.

Finally, in terms of practical applicability beyond standard cylindrical specimens, the same principle can be extended to real parts by evaluating the section properties of the actual load-bearing cross-section where the maximum stress is expected and computing the outer-fiber bending stress with respect to the loading direction. For irregular or non-circular printed sections, obtaining the moment of inertia may not lead to a simple closed-form expression; in such cases, numerical integration of a cross-section or finite element analysis can be used to estimate the section properties and the resulting maximum stress.

7. Conclusions

This study shows that applying ISO 1143:2010 to FFF-printed polymer components using a fully solid circular cross-section can bias the stress level inferred from rotating bending fatigue tests, since the effective stiffness depends on the shell–infill morphology and its deviations from an ideal cylinder. Assuming that FFF specimens have fully solid sections underestimates the maximum stress and may therefore overestimate fatigue life. By introducing and comparing analytical approaches with increasing geometric fidelity, this study demonstrates that a geometry-aware estimation of section properties yields more consistent stress values and improves the comparability of S–N curves across different FFF configurations. Particularly, the Method 4 (AGB) formulation is suitable for horizontally printed cylinders where shell ovalization and non-uniform thickness become critical. From the experimental campaign on PLA, the results also indicate a clear influence of internal morphology, with grid infill providing longer fatigue lives than honeycomb under identical conditions.

From a practical standpoint, the proposed framework can be used to select an appropriate level of geometric detail depending on printing orientation and morphology. Method 1 (ISO) is appropriate only when the specimen is effectively solid. Methods 2 and 3 provide simplified geometry-aware estimates and are most suitable when the cross-section has approximately uniform shell thickness (typically in vertically printed cylinders), with Method 3 preferred when the shell contribution is explicitly considered. Method 4 (AGB) is recommended for horizontally printed cylinders, where ovalization and non-uniform shell thickness govern the critical section and the resulting maximum stress. Obtaining higher geometric fidelity requires additional inputs, such as a more detailed characterization of the printed cross-section, which may not always be available for complex parts. When such information is available, the same principle can be extended to real parts by evaluating the section properties at the expected critical cross-section and computing the maximum outer-fiber stress with respect to the actual loading direction. For non-cylindrical or irregular sections, this evaluation may require numerical section integration or finite element modeling.

The main limitations of the present analytical approaches arise from the simplified representation of infill effectiveness and from the variability inherent to FFF processes. These factors may affect the effective stiffness of the shell–infill system and the identification of the critical section. In addition, simplified approaches that

Accepted Manuscript

neglect the shell may lead to conservative stress estimates, since the outer contours often carry a significant fraction of the bending load. Future work will focus on extending the methodology to more complex geometries and different material systems. It will also investigate how process-related factors, such as interlayer adhesion and printing defects, affect fatigue performance.

Author Contributions: Conceptualization, CBG and JALF; methodology, CBG and JALF; validation, SMB and FBG; formal analysis, CBG, JALF, SMB and FBG; investigation, CBG and JALF; resources, SMB and FBG; data curation, SMB and FBG; writing—original draft preparation, CBG; writing—review and editing, CBG and JALF; visualization, SMB and FBG; supervision, JALF; project administration, CBG and JALF; All authors have read and agreed to the published version of the manuscript.

Acknowledgments

The authors thank the University of Malaga–Andalucia Tech Campus of International Excellence for its contribution to this paper.

Declaration of generative AI and AI-assisted technologies in the writing process

During the preparation of this work the authors used ChatGPT in order to review the grammar of the article and possible formatting and writing errors. After using this tool/service, the authors reviewed and edited the content as needed and take full responsibility for the content of the publication.

References

[1] G. Kharmanda, A Review on Uncertainty Cases in Additively Manufactured Polylactic Acid Using Fused Filament Fabrication Technique, International Journal of Additive-Manufactured Structures (2023). https://doi.org/10.53964/ijams.2023001.

[2] E. García, P.J. Núñez, M.A. Caminero, J.M. Chacón, S. Kamarthi, Effects of carbon fibre reinforcement on the geometric properties of PETG-based filament using FFF additive manufacturing, Compos B Eng 235 (2022) 109766. https://doi.org/10.1016/j.compositesb.2022.109766.

[3] C.P. Paul, K. Dileep, A.N. Jinoop, A.C. Paul, K.S. Bindra, Fused Filament Fabrication for External Medical Devices, in: 2021: pp. 299–322. https://doi.org/10.1007/978-3-030-68024-4_16.

[4] C. Phillips, M. Kortschot, F. Azhari, Material Characterization of Fused Filament Fabrication for Lower-Limb Prosthetic Sockets, in: ASME 2022 Conference on Smart Materials, Adaptive Structures and Intelligent Systems, American Society of Mechanical Engineers, 2022. https://doi.org/10.1115/SMASIS2022-88833.

[5] N. Maqsood, M.D. Zaheer, Fabrication of Cellular Composite Structures with Continuous Fiber Reinforcement and Different Infill Patterns Using Fused Filament Fabrication, Additive Manufacturing Frontiers 3 (2024) 200156. https://doi.org/10.1016/j.amf.2024.200156.

[6] R. Soundararajan, E. Dharunprakash, N. Arjunkumaar, A.D. Gowthamprasath, Appraisal of Mechanical and Tribological Performance of Onyx and Carbon Fiber Composites Produced Through Various Layering Approaches in Continuous Fused Filament Fabricated, Journal of The Institution of Engineers (India): Series D 106 (2025) 215–229. https://doi.org/10.1007/s40033-023-00626-z.

[7] T. Cadiou, F. Demoly, S. Gomes, A hybrid additive manufacturing platform based on fused filament fabrication and direct ink writing techniques for multi-material 3D printing, The International Journal

Accepted Manuscript

of Advanced Manufacturing Technology 114 (2021) 3551–3562. https://doi.org/10.1007/s00170-021-06891-0.

[8] M. Seleznev, J.D. Roy-Mayhew, Bi-metal composite material for plastic injection molding tooling applications via fused filament fabrication process, Addit Manuf 48 (2021) 102375. https://doi.org/10.1016/j.addma.2021.102375.

[9] PL. Ramkumar, T. Rijwani, Additive manufacturing of metals and ceramics using hybrid fused filament fabrication, Journal of the Brazilian Society of Mechanical Sciences and Engineering 44 (2022) 455. https://doi.org/10.1007/s40430-022-03762-x.

[10] C. Belei, S.T. Amancio-Filho, Influence of Raster Orientation and Feeding Rate on the Mechanical Properties of Short Carbon Fiber-Reinforced Polyamide Printed by Fused-Filament Fabrication, 3D Print Addit Manuf 11 (2024) 1921–1929. https://doi.org/10.1089/3dp.2023.0173.

[11] J. Ghorbani, P. Koirala, Y.-L. Shen, M. Tehrani, Eliminating voids and reducing mechanical anisotropy in fused filament fabrication parts by adjusting the filament extrusion rate, J Manuf Process 80 (2022) 651–658. https://doi.org/10.1016/j.jmapro.2022.06.026.

[12] P. Yadav, A. Sahai, R.S. Sharma, Experimental Studies on the Mechanical Behavior of Three-Dimensional PLA Printed Parts by Fused Filament Fabrication, Journal of The Institution of Engineers (India): Series D 104 (2023) 233–245. https://doi.org/10.1007/s40033-022-00403-4.

[13] N. Dialami, M. Chiumenti, M. Cervera, R. Rossi, U. Chasco, M. Domingo, Numerical and experimental analysis of the structural performance of AM components built by fused filament fabrication, International Journal of Mechanics and Materials in Design 17 (2021) 225–244. https://doi.org/10.1007/s10999-020-09524-8.

[14] A. Estefani, L. Távara, Numerical multiscale analysis of 3D printed short fiber composites parts: Filament anisotropy and toolpath effects, Engineering Reports 6 (2024). https://doi.org/10.1002/eng2.12799.

[15] S. Hassanifard, S.M. Hashemi, On the strain-life fatigue parameters of additive manufactured plastic materials through fused filament fabrication process, Addit Manuf 32 (2020) 100973. https://doi.org/10.1016/j.addma.2019.100973.

[16] M.R. Adibeig, M.-A. Saeimi-Sadigh, F. Vakili-Tahami, M.R. Karimani, G. Marami, Quasi-static simulation and fatigue life estimation of fused filament fabrication of polylactic acid specimens using finite element method, J Manuf Process 106 (2023) 202–213. https://doi.org/10.1016/j.jmapro.2023.09.071.

[17] J.A. Travieso-Rodriguez, M.D. Zandi, R. Jerez-Mesa, J. Lluma-Fuentes, Fatigue behavior of PLA-wood composite manufactured by fused filament fabrication, Journal of Materials Research and Technology 9 (2020) 8507–8516. https://doi.org/10.1016/j.jmrt.2020.06.003.

[18] M. Brčić, S. Kršćanski, J. Brnić, Rotating Bending Fatigue Analysis of Printed Specimens from Assorted Polymer Materials, Polymers (Basel) 13 (2021) 1020. https://doi.org/10.3390/polym13071020.

[19] N. Nagengast, T. Scharl, M. Frisch, C. Neuber, H. Ruckdäschel, H.-W. Schmidt, F.K. Fuss, Design for Sustainable Additive Manufacturing (DfsAM): Preparation and Validation of a Transversely Isotropic Simulation Model for FFF Components Made from Virgin and Recycled Polypropylene Filaments, in: 2023 14th International Conference on Mechanical and Intelligent Manufacturing Technologies (ICMIMT), IEEE, 2023: pp. 204–212. https://doi.org/10.1109/ICMIMT59138.2023.10199510.

Accepted Manuscript

[20] S.N. Cerda-Avila, H.I. Medellín-Castillo, J.M. Cervántes-Uc, A. May-Pat, A. Rivas-Menchi, Fatigue experimental analysis and modeling of fused filament fabricated PLA specimens with variable process parameters, Rapid Prototyp J 29 (2023) 1155–1165. https://doi.org/10.1108/RPJ-10-2022-0354.

[21] ISO, ISO 1143:2010 Standard. Metallic materials — Rotating bar bending fatigue testing, in: ISO, 2010. https://www.iso.org/standard/41875.html (accessed December 19, 2019).

[22] C. Bermudo Gamboa, S. Martín-Béjar, F. Bañón García, L. Sevilla Hurtado, Enhancing Fatigue Resistance of Polylactic Acid through Natural Reinforcement in Material Extrusion, Polymers (Basel) 16 (2024) 2422. https://doi.org/10.3390/polym16172422.

[23] M. Azadi, A. Dadashi, Experimental fatigue dataset for additive-manufactured 3D-printed Polylactic acid biomaterials under fully-reversed rotating-bending bending loadings, Data Brief 41 (2022) 107846. https://doi.org/10.1016/J.DIB.2022.107846.

[24] C. Bermudo Gamboa, S. Martín-Béjar, J. Trujillo Vilches, L. Sevilla Hurtado, Influence of printing parameters and short carbon fibre reinforcement on fatigue behavior, dimensional accuracy and macrogeometrical deviations of polylactic acid in material extrusion, Compos Sci Technol 242 (2023) 110205. https://doi.org/10.1016/j.compscitech.2023.110205.

[25] M. Azadi, A. Dadashi, S. Dezianian, M. Kianifar, S. Torkaman, M. Chiyani, High-cycle bending fatigue properties of additive-manufactured ABS and PLA polymers fabricated by fused deposition modeling 3D-printing, Forces in Mechanics 3 (2021) 100016. https://doi.org/10.1016/J.FINMEC.2021.100016.

[26] A. Dadashi, M. Azadi, Experimental bending fatigue data of additive-manufactured PLA biomaterial fabricated by different 3D printing parameters, Progress in Additive Manufacturing (2022) 1–9. https://doi.org/10.1007/S40964-022-00327-1/TABLES/4.

[27] F.J. Trujillo, S. Martín-Béjar, C. Bermudo, L. Sevilla, Fatigue test bench manufacturing by reusing a parallel lathe, in: Advances in Transdisciplinary Engineering, IOS Press BV, 2018: pp. 15–20. https://doi.org/10.3233/978-1-61499-902-7-15.

[28] C.B. Gamboa, S. Martín-Béjar, F.J.T. Vilches, M.H. Fernández, L.S. Hurtado, Fatigue Behavior Analysis in Reinforced PLA Parts Manufactured by FDM, Key Eng Mater 956 (2023) 91–98. https://doi.org/10.4028/P-OCVW8O.

[29] C. Bermudo Gamboa, S. Martín Béjar, F.J. Trujillo Vilches, L. Sevilla Hurtado, Geometrical analysis in material extrusion process with polylactic acid (PLA)+carbon fiber, Rapid Prototyp J 29 (2022) 21–39. https://doi.org/10.1108/RPJ-09-2022-0294/FULL/PDF.

[30] C. Bermudo Gamboa, S. Martín Béjar, F.J. Trujillo Vilches, L. Sevilla Hurtado, Geometrical analysis in material extrusion process with polylactic acid (PLA)+carbon fiber, Rapid Prototyp J 29 (2022) 21–39. https://doi.org/10.1108/RPJ-09-2022-0294/FULL/PDF.

[31] J. Lee, A. Huang, Fatigue analysis of FDM materials, Rapid Prototyp J 19 (2013) 291–299. https://doi.org/10.1108/13552541311323290.

[32] J.F. Mandell, Fatigue Behavior of Short Fiber Composite Materials, Composite Materials Series 4 (1991) 231–337. https://doi.org/10.1016/B978-0-444-70507-5.50011-1.

[33] G. Gomez-Gras, R. Jerez-Mesa, J.A. Travieso-Rodriguez, J. Lluma-Fuentes, Fatigue performance of fused filament fabrication PLA specimens, Mater Des 140 (2018) 278–285. https://doi.org/10.1016/J.MATDES.2017.11.072.

Accepted Manuscript

[34] G. Gomez-Gras, R. Jerez-Mesa, J.A. Travieso-Rodriguez, J. Llumà-Fuentes, D. Puig, Fatigue lifespan study of PLA parts obtained by additive manufacturing, Procedia Manuf 13 (2017) 872–879. https://doi.org/10.1016/J.PROMFG.2017.09.146.

[35] M.S.A. Parast, A. Bagheri, A. Kami, M. Azadi, V. Asghari, Bending fatigue behavior of fused filament fabrication 3D-printed ABS and PLA joints with rotary friction welding, Progress in Additive Manufacturing 7 (2022) 1345–1361. https://doi.org/10.1007/s40964-022-00307-5.

Accepted Manuscript